Long-Range Hybrid Plasmonic Disk Resonators for mW Bistability and Self-Pulsation

Odysseas Tsilipakos *Member, IEEE*, Thomas Christopoulos, and Emmanouil E. Kriezis *Senior Member, IEEE*

***Abstract*—A side-coupled disk-waveguide system based on a long-range hybrid plasmonic waveguiding configuration is theoretically investigated for Kerr bistability and self-pulsation. The nonlinear response is studied with a theoretical framework combining perturbation theory and temporal coupled-mode theory, where all relevant effects, including two-photon absorption (TPA) as well as free-carrier dispersion (FCD) and absorption (FCA), are taken into account. We show that bistable operation with input powers as low as 40 mW is possible; a consequence of the significant reduction in resistive losses made possible by the long-range waveguiding principle. The effect of TPA, FCD, and FCA on the nonlinear response is thoroughly assessed and it is shown that carrier lifetime must drop to 8 ps in order to suppress free-carrier effects and obtain a high-quality bistable response, which is subsequently exploited for demonstrating ultrafast memory operation with low power requirements and high extinction ratio between states. Finally, by appropriate tuning of the carrier lifetime, FCD can lead to self-pulsation. The operating regimes in the detuning-power space are identified and the characteristics of the spontaneous oscillation discussed.**

***Index Terms*—Nonlinear optics, optical bistability, plasmonics, long-range hybrid plasmonic waveguides.**

I. Introduction

NONLINEAR phenomena in guided-wave plasmonics are attracting increasing interest, due to their potential for implementing integrated components performing elaborate functions [1]. In particular, exploiting the third order susceptibility, $\chi^{(3)}$, can be a favorable approach towards all-optical devices with ultrafast response. Interestingly, the combination of $\chi^{(3)}$ nonlinearity and optical feedback in resonant nonlinear structures can lead to bistable behavior. In turn, this opens a pathway for implementing memory [2], switching [3], and logic-gate functions [4], [5].

Initially, bistability studies in plasmonics revolved around two-dimensional geometries with the metal-insulator-metal waveguide. Addressing the need for practical, three-dimensional bistable components, we have recently examined the manifestation of optical bistability (BI) with nonlinear traveling- [6] and standing-wave [7] resonators made of hybrid plasmonic waveguides (HPWs), whose tight mode confinement renders them a prime candidate for nonlinear applications. Although the potential of plasmonic bistable structures has been highlighted, the power requirements for bistable switching remain high ($>$1 W); a direct consequence of the lossy nature of plasmonic structures.

In this work, we attempt to lower the power requirements of integrated HPW-based components for Kerr bistability. To this end, we apply the concept of long-range waveguiding, i.e., we mirror the waveguide structure in order to create a symmetric HPW configuration supporting modes with enhanced propagation length [8], [9]. The resulting long-range hybrid plasmonic waveguide (LRHPW) features significantly reduced propagation (resistive) losses, while retaining the nanoscale mode confinement of the original HPW. Consequently, resonant nonlinear systems based on the LRHPW are expected to exhibit reduced power requirements for bistable operation. This is demonstrated with a system consisting of a nonlinear disk resonator side-coupled to a bus waveguide. We show that through proper design bistable switching can be accomplished with mW input powers.

For studying the optical response we employ a theoretical framework combining perturbation theory and temporal coupled-mode theory (CMT), fed with full-wave simulations of the *linear* system performed with the three-dimensional vectorial finite element method (3D-VFEM). All relevant phenomena are taken into account, including two photon absorption (TPA) taking place in the silicon layer of the structure and the effect of TPA-generated free carriers (FCs). We find that although the effect of TPA is negligible, free-carrier induced dispersion (FCD) and absorption (FCA) dramatically affect the nonlinear response. Kerr-induced bistability can still be observed, provided that carrier lifetime drops to approximately 10 ps. Such carrier lifetimes are comparable with the cavity photon lifetime. We, thus, investigate the self-pulsing behavior of the system, as well.

The paper is organized as follows. The nonlinear LRHPW is presented in Section II. In Section III the LRHPW-based disk-waveguide system is designed for Kerr bistability, targeting minimum power threshold and maximum extinction ratio (ER) between bistable states. The theoretical framework is introduced and, by momentarily neglecting FCD and FCA, a system of two polynomial equations describing the CW nonlinear response is derived. The effect of FCs on Kerr bistability is thoroughly investigated in Section III-C. Efficient bistable operation with mW input power is demonstrated for a carrier lifetime of 8 ps. As carrier lifetime becomes comparable with the cavity photon lifetime, self-pulsation (SP) can be observed. Section IV is devoted to the study of this phenomenon. Finally, a discussion is provided in the concluding Section V.

Manuscript received November xx, 2015. This work has been co-financed by the European Union (European Social Fund) and Greek national funds through the Operational Program "Education and Lifelong Learning" of the National Strategic Reference Framework: Research Funding Program THALES "Reinforcement of the interdisciplinary and/or inter-institutional research and innovation" (Project ANEMOS).

O. Tsilipakos, T. Christopoulos, and E. E. Kriezis are with the Department of Electrical and Computer Engineering, Aristotle University of Thessaloniki, Thessaloniki GR-54124, Greece. (e-mail: otsilipa@auth.gr)

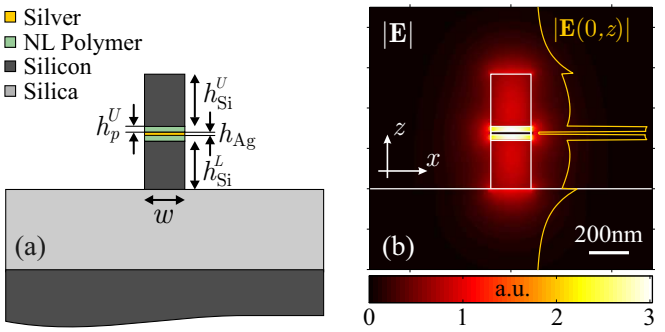

Fig. 1. (a) Nonlinear LRHPW. The nonlinear polymer DDMEBT occupies the low-index regions between silver and silicon layers. The heights of the five layers comprising the guiding ridge are $\{h^L_{\rm Si}, h^L_p, h_{\rm Ag}, h^U_p, h^U_{\rm Si}\} = \{243, 25, 15, 25, 260\}$ nm. $h^L_{\rm Si}$ has been properly tuned to render the mode perfectly symmetric, despite the asymmetric nature of the structure due to the SiO_2 substrate. The waveguide width w is 200 nm. (b) Electric field norm for the long-range mode at 1.55 μm. The mode is symmetric along the z-axis, i.e., the E-field norm is equally strong on either side of the silver layer.

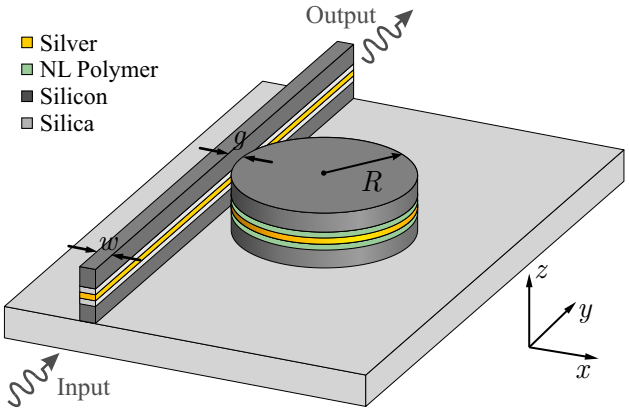

Fig. 2. Nonlinear disk resonator side-coupled to a bus waveguide through coupling gap g. The implementation is based on the LRHPW of Fig. 1.

II. Nonlinear Long-Range Hybrid Plasmonic Waveguide

Long-range modes were first studied with the stripe plasmonic waveguide [10]. The same principle of a symmetric waveguiding environment supporting a long-range mode was some years later transferred to HPWs [8], [9], in order to take advantage of the tight confinement offered by the metal/low-index-gap/high-index-semiconductor layer configuration. In practical situations where the cladding is different from the substrate, the waveguiding configuration is not exactly symmetric. This has a detrimental effect on propagation loss, compromising the long-range nature of the supported mode. However, the propagation length can be restored to the levels of the symmetric structure by following a procedure of symmetrizing the mode (field) profile by varying certain waveguide dimensions [11], [12].

The cross-section of the nonlinear LRHPW used in this work is depicted in Fig. 1(a). It is the long-range counterpart of the HPW employed in [6], [7] and consists of two low-index, nonlinear polymer regions sandwiched between metal and high-index semiconductor layers. More specifically, the semiconductor is silicon and the metal silver since it exhibits lower resistive losses compared to other alternatives. DDMEBT [13] is chosen as the nonlinear polymer, being highly nonlinear ($n_2 = 1.7 \times 10^{-17}$ m^2/W) and moreover compatible with nanophotonic integration. At 1.55 μm the linear refractive indexes for the materials involved are $n_{\rm Si} = 3.48$, $n_{\rm Ag} = 0.145 - j11.4$ [14], $n_p = 1.8$, and $n_{\rm SiO_2} = 1.45$.

Regarding waveguide dimensions, the waveguide width w is 200 nm and the heights of the five layers comprising the guiding ridge are $\{h^L_{\rm Si}, h^L_p, h_{\rm Ag}, h^U_p, h^U_{\rm Si}\} = \{243, 25, 15, 25, 260\}$ nm. The 200-nm width ensures that the underlying HPW is single mode. The 15-nm-thick metal layer is sufficiently thin to guarantee large propagation lengths while remaining technologically feasible [15]. Polymer layers are both 25-nm thick so that the aggregate thickness equals 50 nm, as in [6]. Notice that the lower silicon layer has been properly tuned from the nominal thickness of 260 nm ($h^L_{\rm Si} = 243$ nm) to render the mode profile symmetric.

This can be verified by observing Fig. 1(b) where the supported long-range mode is depicted. Indeed, after adjusting $h^L_{\rm Si}$ the mode becomes perfectly symmetric along the z-axis, i.e., the E-field norm is equally strong on either side of the silver layer. Note that the LRHPW can be considered a composite waveguide consisting of two HPWs, coupled through their common metal layer (provided it is sufficiently thin to permit field tunnelling). As such, it supports two "supermodes" with opposite field symmetries [12]. The long-range mode depicted in Fig. 1(b) is characterized by a symmetric distribution of the E_z component along the vertical direction (z-axis), whereas the other "supermode" (not shown) is characterized by an antisymmetric E_z distribution. The latter suffers very high propagation losses and is not of practical interest for bistability applications.

Returning to the long-range mode depicted in Fig. 1(b), the effective index at 1.55 μm is $1.996 - j1.112 \times 10^{-4}$. The imaginary part corresponds to a propagation length of 1110 μm, a spectacular improvement compared to the 80 μm of the HPW in [6]. Importantly, this improvement is not accompanied by a drastic change in the mode area. More specifically, we calculate $A_{\rm eff} = 0.069$ μm^2 instead of 0.052 μm^2 [6]. On the whole, the LRHPW of Fig. 1(a) combines low loss with nanoscale confinement and is therefore particularly well suited to our application. Finally, regarding waveguide nonlinearity, by employing the definition in [16] we find $\gamma_{\rm wg} = 1485 - j11.4$ W^{-1}m^{-1}. Nonlinearity stems almost exclusively from the nonlinear polymer, due to its higher nonlinear index than Si ($n_2^{\rm Si} = 2.5 \times 10^{-18}$ m^2/W) and the better overlap with the supported mode [Fig. 1(b)]. Specifically, the contribution of Si to the real part of $\gamma_{\rm wg}$ is only 3%. However, silicon manifests itself through the imaginary part of $\gamma_{\rm wg}$, which accounts for TPA ($\beta^{\rm Si}_{\rm TPA} = 5 \times 10^{-12}$ m/W) and gives rise to free carrier effects (FCEs).

III. Disk-Waveguide System for Kerr Bistability

The physical system under study is depicted in Fig. 2. It consists of a disk resonator based on the nonlinear LRHPW of Fig. 1 side-coupled with a standard LRHPW (silica occupying the low-index regions instead of DDMEBT). The waveguide

width is 200 nm. To study the *nonlinear* response of the disk-waveguide system we employ a CMT framework where nonlinearity is introduced by utilizing perturbation theory [6], [17], [18]. The resonator is treated as being lumped; dependence on spatial coordinates is absent and the physical system is hidden in the coefficients entering in the CMT equation. They are specified by conducting full-wave simulations of the *linear* system, carried out with the 3D-VFEM [19]. Following this approach we avoid tedious nonlinear full-wave simulations, saving valuable resources without, however, sacrificing the accuracy of the results [18], [20].

A. Coupled-Mode Theory Framework

A CMT framework for modeling Kerr-induced bistability in photonic crystal structures was originally described in [17]. In [21] this framework was extended to include TPA and the resulting free-carrier effects (FCD and FCA) in the context of silicon-on-insulator microring resonators. Since a Si layer is present in our structure, all of these effects should be taken into account. However, here we will first outline the framework by including TPA but *not* FCEs. This will allow us to derive a system of two polynomial equations for describing the CW nonlinear response when FCEs are negligible. Note that due to the presence of TPA it is no longer possible to end up with a *single* polynomial equation, as in [6]. However, the system of two polynomial equations is still useful and moreover permits us to derive a *closed-form* expression for the detuning threshold for bistability.

We start from a CMT equation identical with the one in [6], with the exception of an extra term accounting for TPA:

$$\frac{\mathrm{d}a}{\mathrm{d}t} = j(\omega_0+\Delta\omega)a - \left(\frac{1}{\tau_i}+\frac{1}{\tau_e}+\frac{1}{\tau_{\mathrm{TPA}}}\right)a + j\sqrt{\frac{2}{\tau_e}}s_i, \quad (1a)$$

$$s_t = s_i + j\sqrt{\frac{2}{\tau_e}}a. \quad (1b)$$

In (1) τ_i and τ_e denote cavity photon lifetimes corresponding to *linear* intrinsic losses (radiation and resistive) and external (coupling) losses, respectively. The respective quality factors are given by $Q = \omega_0\tau/2$. $\Delta\omega$ is the Kerr-induced nonlinear frequency shift perturbing the resonant frequency ω_0. Furthermore, s_i and s_t denote incident and transmitted wave amplitudes, normalized so that $|s|^2$ expresses guided power. In the same way, the cavity amplitude a is normalized so that $|a|^2$ is the energy stored in the resonator, W. On resonance, where electric and magnetic energies are equal, the stored energy is given by $(\varepsilon_0/2)\iiint_V n^2(\mathbf{r})\,|\mathbf{E}_0|^2\,\mathrm{d}V$. Note that unlike τ_i and τ_e, τ_{TPA} is not constant; it depends on the stored energy since TPA is a *nonlinear* intrinsic loss mechanism. Thus, when solving (1) for constructing the hysterisis loop one has to bear in mind that the stored energy is hidden not only in $\Delta\omega = -\gamma_{\mathrm{Kerr}}W$ (notice the minus sign), but in $\tau_{\mathrm{TPA}}^{-1} = \gamma_{\mathrm{TPA}}W$ as well. The nonlinear parameters γ, measured in $\mathrm{W}^{-1}\mathrm{s}^{-2}$, are given by

$$\gamma_{\mathrm{Kerr}} = \frac{1}{4}\left(\frac{\omega_0}{c_0}\right)^3 c_0\omega_0\kappa_{\mathrm{Kerr}}n_2^{\max}, \quad (2a)$$

$$\gamma_{\mathrm{TPA}} = \frac{1}{8}\left(\frac{\omega_0}{c_0}\right)^3 c_0^2\kappa_{\mathrm{TPA}}\beta_{\mathrm{TPA}}^{\max}. \quad (2b)$$

Obviously, γ_{Kerr} and γ_{TPA} are the *resonator* (3D) counterparts of real and imaginary parts of the *waveguide* (2D) nonlinear parameter γ_{wg}. The *dimensionless* nonlinear feedback parameters κ_{Kerr} and κ_{TPA} appearing in (2) are defined as

$$\kappa_{\mathrm{Kerr}} \triangleq \left(\frac{c_0}{\omega_0}\right)^3 \frac{\frac{1}{3}\iiint_V n_2n^2\left[|\mathbf{E}_0\cdot\mathbf{E}_0|^2+2|\mathbf{E}_0|^4\right]\mathrm{d}V}{\left[\frac{1}{2}\iiint_V n^2|\mathbf{E}_0|^2\,\mathrm{d}V\right]^2 n_2^{\max}}, \quad (3a)$$

$$\kappa_{\mathrm{TPA}} \triangleq \left(\frac{c_0}{\omega_0}\right)^3 \frac{\frac{1}{3}\iiint_V \beta_{\mathrm{TPA}}n^2\left[|\mathbf{E}_0\cdot\mathbf{E}_0|^2+2|\mathbf{E}_0|^4\right]\mathrm{d}V}{\left[\frac{1}{2}\iiint_V n^2|\mathbf{E}_0|^2\,\mathrm{d}V\right]^2 \beta_{\mathrm{TPA}}^{\max}}, \quad (3b)$$

with $\mathbf{E}_0$ denoting the unperturbed electric field in the structure (the coordinate dependence is suppressed). Note that the integrations in the nominator of (3a) and (3b) will be primarily performed in polymer and semiconductor layers, respectively, since DDMEBT is almost exclusively responsible for the Kerr-induced frequency shift (Si contribution to κ_{Kerr} is 3.8%) but TPA takes place in silicon. Therefore, κ_{Kerr} (κ_{TPA}) measures the degree of overlap between the supported mode and the polymer (semiconductor) material. Note also that κ_{Kerr} is inversely proportional to the effective mode volume [6].

As already mentioned, in the steady state (1) can reduce to a system of polynomial equations. To this end, we follow a procedure similar to the one in [6]. More specifically, making use of the standard definition for the quality factor we can associate the linear intrinsic resonator losses (radiation and resistive), P_i, with the stored energy through

$$W = Q_i\frac{P_i}{\omega_0} = Q_i\frac{P_{\mathrm{in}}-P_{\mathrm{out}}-P_{\mathrm{TPA}}}{\omega_0}. \quad (4)$$

Note that here P_i is not simply $P_{\mathrm{in}}-P_{\mathrm{out}}$ as in [6], since TPA losses are also present. The power dissipated due to TPA in the infinitesimal volume $\mathrm{d}V$ can be expressed as

$$\begin{aligned}\mathrm{d}P_{\mathrm{TPA}} &= \frac{1}{2}\,\mathrm{Re}\{\mathbf{E}_0^*\cdot j\omega\mathbf{P}^{(3)}\}\mathrm{d}V \\ &= \frac{\varepsilon_0^2c_0^2n^2}{12}\beta_{\mathrm{TPA}}\left[|\mathbf{E}_0\cdot\mathbf{E}_0|^2+2|\mathbf{E}_0|^4\right]\mathrm{d}V.\end{aligned} \quad (5)$$

Integrating over the resonator volume we can write

$$P_{\mathrm{TPA}} = 2\gamma_{\mathrm{TPA}}W^2 = 2\gamma_{\mathrm{TPA}}|a|^4. \quad (6)$$

Now, assuming a harmonic ($\exp\{j\omega t\}$) time dependence, using (4) in both (1a) and (6), and following a normalization procedure identical to the one in [6], we can arrive at the system of polynomial equations

$$\frac{p_{\mathrm{out}}}{p_{\mathrm{in}}} = \frac{(\delta+p_i)^2+(1-r_Q+r_{\mathrm{TPA}}p_i)^2}{(\delta+p_i)^2+(1+r_Q+r_{\mathrm{TPA}}p_i)^2}, \quad (7a)$$

$$p_{\rm TPA} = r_{\rm TPA} p_i^2, \tag{7b}$$

where $p_i = p_{\rm in} - p_{\rm out} - p_{\rm TPA}$ and all power levels have been normalized with respect to

$$P_0^{\rm Kerr} = \frac{2}{\left(\frac{\omega_0}{c_0}\right)^2 \kappa_{\rm Kerr}\, Q_i^2\, n_2^{\rm max}} = \frac{2}{\tau_i^2 \gamma_{\rm Kerr}}, \tag{8}$$

the characteristic power of the system associated with the threshold for Kerr bistability. In (7) $\delta = \tau_i(\omega - \omega_0)$ is the normalized detuning, $r_Q = \tau_i/\tau_e = Q_i/Q_e$ the internal to external quality factor ratio, and $r_{\rm TPA}$ is defined as

$$r_{\rm TPA} = \frac{\gamma_{\rm TPA}}{\gamma_{\rm Kerr}} = \frac{\kappa_{\rm TPA}}{\kappa_{\rm Kerr}} \frac{\beta_{\rm TPA}^{\rm max}}{2k_0 n_2^{\rm max}}. \tag{9}$$

Equations (7) can be readily used for constructing the hysterisis loop: by appointing a specific value to $p_{\rm in}$, a system of two equations with two unknowns ($p_{\rm out}$ and $p_{\rm TPA}$) is formed. In addition, through (7a) we can specify a closed-form expression for the detuning threshold for bistability. Following the procedure outlined in [7], i.e., setting $\partial p_{\rm in}/\partial p_{\rm out} = 0$ and requiring a positive discriminant, we arrive at

$$\delta < -\frac{(1+r_Q)(\sqrt{3}+r_{\rm TPA})}{1-\sqrt{3}\,r_{\rm TPA}}. \tag{10}$$

Note that in the absence of TPA, $r_{\rm TPA} = 0$, (10) reduces to $\delta < -(1+r_Q)\sqrt{3}$, in agreement with [6].

B. System Design and Performance

In this Section, we design the physical system (i.e., determine the disk radius R and coupling gap g, Fig. 2) for optimum performance. In particular, we are interested in minimum threshold for bistability and maximum ER between bistable states. As thoroughly discussed in [6], the first requirement is met by minimizing P_0 and retaining the detuning δ close to the respective threshold, whereas the second by satisfying the critical coupling condition. When only *linear* intrinsic losses are present, critical coupling corresponds to the condition $r_Q = 1$ ($Q_e = Q_i$); in the presence of TPA (a *nonlinear* intrinsic loss mechanism) it is modified to $Q_e^{-1} = Q_i^{-1} + Q_{\rm TPA}^{-1}$.

We first focus on minimizing the system characteristic power $P_0^{\rm Kerr}$, or, equivalently, maximizing the $\kappa_{\rm Kerr} Q_i^2$ product [Eq. (8)]. To this end, we perform eigenvalue simulations of the uncoupled resonator (in the linear regime), varying the disk radius in order to identify the optimum value. As R increases, radiation losses are reduced leading to higher values of Q_i. On the other hand, $\kappa_{\rm Kerr}$ decreases as the mode occupies larger volumes ($\kappa \propto V_{\rm eff}^{-1}$). We are, thus, looking for the radius offering the best compromise between the two competing trends. The described procedure is performed for the *symmetric* structure (disk suspended in air), i.e., we momentarily ignore the silica substrate in order to avoid a separate mode symmetrization procedure (like the one performed for the waveguide in Section II) for each radius value.

The results are depicted in Fig. 3. Each marker corresponds to a resonant mode with different azimuthal order m, marked in Fig. 3(b). Note that for each mode we have adjusted the radius value in order to center the resonance within ± 2 nm

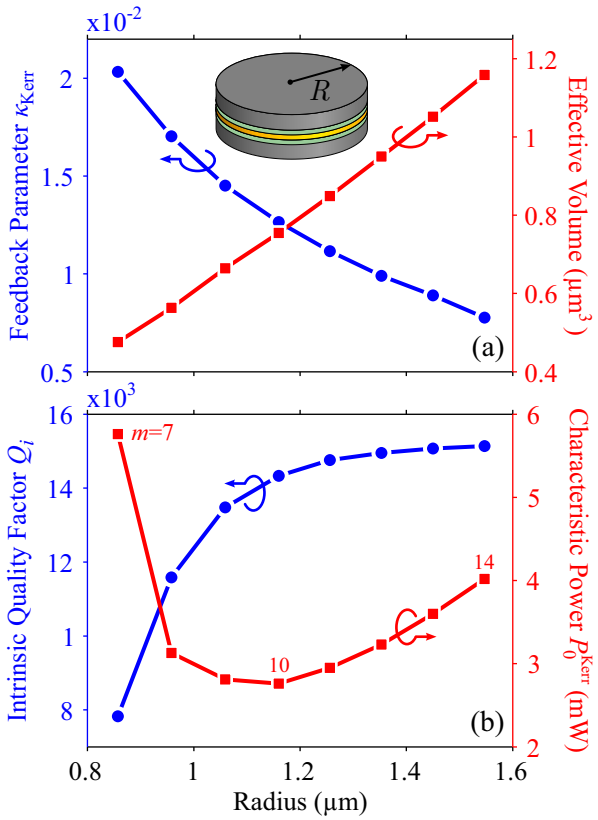

Fig. 3. Uncoupled disk resonator based on the nonlinear LRHPW, modeled with the 3D-VFEM as an eigenvalue problem. The structure is symmetric, i.e., no substrate is considered. (a) Nonlinear feedback parameter $\kappa_{\rm Kerr}$ and effective mode volume $V_{\rm eff}$, as well as (b) intrinsic quality factor Q_i and characteristic power $P_0^{\rm Kerr}$ for the resonant modes of azimuthal order $m = 7 - 14$. The optimum radius is 1.16 μm ($m = 10$) and the corresponding characteristic power is only 2.75 mW.

from 1.55 μm. Observing Fig. 3(a), one can readily verify that $\kappa_{\rm Kerr}$ decreases with radius, being inversely proportional to the effective mode volume. The opposite is true for Q_i, Fig. 3(b), as anticipated. Minimum characteristic power is attained with a radius of 1.16 μm corresponding to the $m = 10$ resonance ($\lambda_{\rm res} = 1552$ nm). It is only 2.75 mW, as can be verified by plugging $\kappa_{\rm Kerr} = 1.27 \times 10^{-2}$ and $Q_i = 14330$ in (8). Note that this power level is significantly reduced compared with the nonlinear HPW-based disk in [6] (215 mW). Applying the long-range concept has resulted in much lower resistive losses, translating into higher quality factors for the resonator.

We now switch to the asymmetric structure and look for the $m = 10$ resonance, specified as the optimum. The presence of the silica substrate renders the supported mode asymmetric, having a detrimental effect on the quality factor. As in the waveguide case (Section II), by varying the thickness of the lower Si layer we can symmetrize the mode profile along the vertical direction (z-axis) and restore resistive loss to the symmetric structure level. Specifically, the height required for this purpose is 250 nm, as demonstrated in Fig. 4 where the resonant mode is plotted. However, radiation loss cannot be restored (the silica/Si index contrast is weaker than the air/Si contrast, translating into increased radiation losses for the asymmetric disk structure). On the whole, even after the

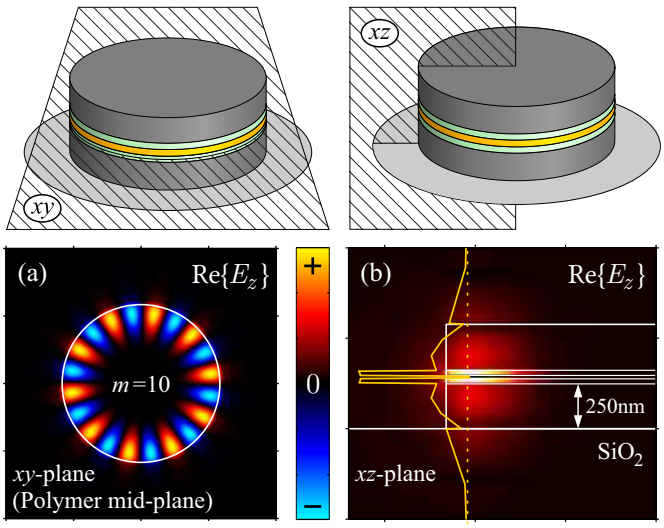

Fig. 4. Resonant mode of the asymmetric disk structure (i.e., with silica substrate) after the mode symmetrization process (lower Si height: 250 nm). The disk radius is $R = 1.158$ μm and the resonant wavelength 1550 nm ($m = 10$). Real part of E_z (dominant electric field component) (a) at the xy-plane slicing the lower polymer layer in half and (b) at the xz-plane containing the resonator axis. Notice the symmetric mode profile. For the illustrated mode $\kappa_{\rm Kerr} = 1.26 \times 10^{-2}$, $Q_i = 10720$, and $P_0^{\rm Kerr} = 5$ mW.

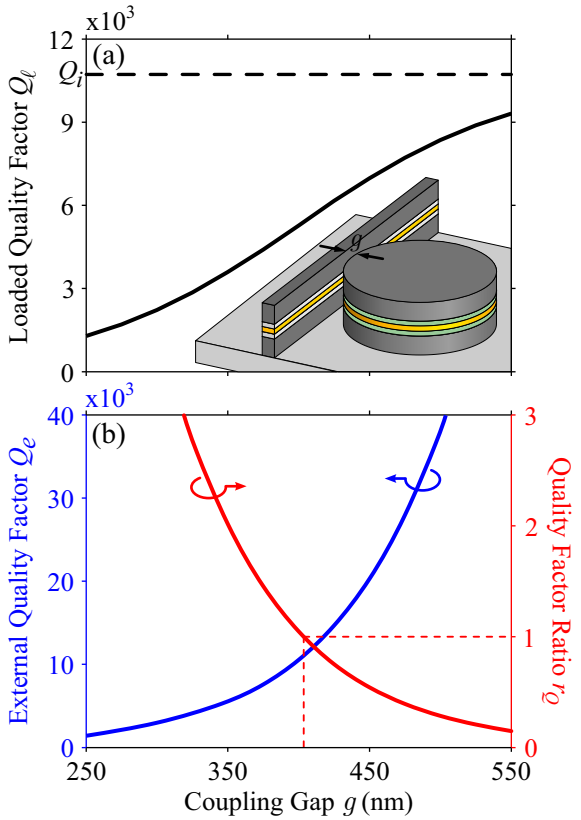

Fig. 5. Nonlinear LRHPW disk resonator coupled to LRHPW bus waveguide. The 3D-VFEM is employed for performing eigenvalue simulations in the linear regime. (a) Loaded quality factor Q_ℓ versus coupling gap g. The unloaded (intrinsic) value is marked with a dashed line. (b) External quality factor Q_e and quality factor ratio $r_Q = Q_i/Q_e$ versus coupling gap g. The $r_Q = 1$ condition is met for $g = 400$ nm.

symmetrization process, the intrinsic quality factor of the $m = 10$ resonant mode drops to 10720, instead of 14330. As a result, the characteristic power of the asymmetric structure becomes 5 instead of 2.75 mW; still, this power level is quite low and well within limits for telecom applications. Note that the disk radius has been adjusted to $R = 1.158$ μm, with the corresponding resonant frequency falling at exactly 1.55 μm.

By observing Fig. 4(b) one can readily verify that the modes of the disk we are interested in are symmetric with respect to the vertical direction (z-axis), as was the case with the waveguide mode in Section II. Again, it is these modes that exhibit reduced propagation losses and, consequently, high quality factors. In the coupled system, the symmetric mode of the disk can only couple to the symmetric mode of the waveguide; coupling with an antisymmetric mode is not permitted since the aggregate (spatial) overlap of the evanescent tails would be zero.

Let us now specify the optimum coupling gap. Since we cannot directly satisfy the modified critical coupling condition ($Q_{\rm TPA}$ depends on the stored energy), we are seeking the gap value that corresponds to $r_Q = 1$ as a starting point for obtaining high ERs between bistable states. If needed, we can further tune the coupling gap, until the desired ER is reached. Again, we perform eigenvalue simulations in the linear regime with the 3D-VFEM. From the imaginary part of the complex eigenfrequency we can extract the loaded quality factor, Q_ℓ. It is plotted in Fig. 5(a) for gap values in the range $250-550$ nm. Naturally, as g increases the resonator-waveguide coupling becomes weaker and Q_ℓ increases approaching the unloaded value (10720) marked with a dashed line. In Fig. 5(b) we plot the external quality factor determined through $Q_e^{-1} = Q_\ell^{-1} - Q_i^{-1}$ and the quality factor ratio $r_Q = Q_i/Q_e$. The $r_Q = 1$ condition is satisfied for $g = 400$ nm.

We complete the design process by specifying the normalized detuning. As already mentioned, δ must be kept close to the respective threshold for bistability manifestation at low input powers [6]. In our case, $r_{\rm TPA} = 0.0095$ (TPA is weak since the mode overlaps primarily with the polymer layers) and $\delta_{\rm th} = -3.54 \approx -2.05\sqrt{3}$ [Eq. (10)]. We therefore set $\delta = -5.55 \approx 1.57\delta_{\rm th}$, meaning that the operating wavelength should be 400 pm higher than the resonant wavelength of the unperturbed resonator, i.e., equal to 1550.4 nm.

Having designed the physical system, we assess its performance. The bistability curve is plotted in Fig. 6. Notice that the effect of TPA in our case is negligible, as can be verified by the additional curve calculated by setting $r_{\rm TPA} = 0$. The hysterisis loop appears for an input power of approximately 28 mW ($5.6P_0^{\rm Kerr}$). Just after the onset of bistability there is an input power level that leads to *almost* vanishing transmission (point A′). Since the coupling gap was designed to satisfy $r_Q = 1$, it would be exactly zero if TPA was absent (only then does $r_Q = 1$ correspond to critical coupling). However, as is evident from Fig. 6, when TPA is weak the prescription $r_Q = 1$ guarantees very high ERs (though not infinite). In Section III-C we will show how we can obtain arbitrarily high ERs between bistable states by further tuning (increasing) the r_Q value in order to account for nonlinear intrinsic loss mechanisms (TPA

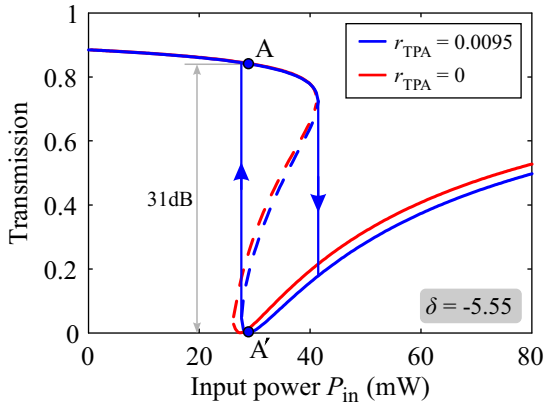

Fig. 6. Bistability curve for the optimum disk-resonator system ($R = 1.158$ μm, $g = 400$ nm). The operating wavelength is 1550.4 nm, 400 pm higher than the resonant wavelength of the unperturbed resonator. Bistability manifests for an input power of approximately 28 mW. Two photon absorption is weak ($r_{\rm TPA} = 0.0095$) and has a negligible effect on the bistability curve. The maximum ER is measured between points A, A' and equals 31 dB.

and FCA) and satisfy the modified critical coupling condition.

C. Effect of Free Carriers

In Sections III-A and III-B the effect of free carriers was deliberately overlooked for the purpose of deriving closed-form expressions for the CW response and the detuning threshold. The weak overlap of the resonant mode with the Si regions where carriers are generated and the marginal effect of TPA itself on the bistability loop (Fig. 6) could perhaps imply that FCEs would not significantly affect the nonlinear response. However, as will become evident this is not the case.

The presence of carriers results in index modulation (FCD) and absorption (FCA). These effects can be incorporated in the CMT framework of Section III-A following the procedure outlined in the appendix. Only the resulting equations (after appropriate normalizations) are shown here, for CW

$$\begin{aligned} j2\sqrt{r_Q}\tilde{\psi}_i =& j\left(\delta + |\tilde{u}|^2 - r_{\rm FCD}|\tilde{u}|^4\right)\tilde{u} \\ &+ \left(1 + r_Q + r_{\rm TPA}|\tilde{u}|^2 + r_{\rm FCA}|\tilde{u}|^4\right)\tilde{u}, \end{aligned} \tag{11}$$

and pulsed operation

$$\begin{aligned} \frac{{\rm d}\tilde{u}}{{\rm d}t'} =& j\left(-\delta - |\tilde{u}|^2 + r_{\rm FCD}^{\rm dyn}(\bar{n})\bar{n}\right)\tilde{u} \\ &- \left(1 + r_Q + r_{\rm TPA}|\tilde{u}|^2 + r_{\rm FCA}^{\rm dyn}\bar{n}\right)\tilde{u} + j2\sqrt{r_Q}\tilde{\psi}_i, \end{aligned} \tag{12a}$$

$$\frac{{\rm d}\bar{n}}{{\rm d}t'} = -\frac{\bar{n}}{\tau_c'} + |\tilde{u}|^4, \tag{12b}$$

where quantities with a tilde ($\tilde{u}$, $\tilde{\psi}$) denote envelope functions. Equations (11), (12) are complemented with the normalized version of (1b): $\tilde{\psi}_t = \tilde{\psi}_i + j\sqrt{r_Q}\tilde{u}$. Notice that in dynamic conditions apart from the CMT equation an additional rate equation for specifying the (normalized) carrier density, $\bar{n}$, must be solved [Eq. (12b)]. Regarding the parameters appearing in (11) and (12), the values calculated for the system under study are compiled in Table I. Note that quantities $r_{\rm FCD}$, $r_{\rm FCA}$ depend on τ_c. The values included are calculated for $\tau_c^{\rm ref} = 8$ ps. However, one can readily obtain values for a different carrier lifetime by multiplying with $\tau_c/\tau_c^{\rm ref}$, since, as shown in the appendix, $r_{\rm FCD/FCA}$ are proportional to τ_c. In addition, $r_{\rm FCD}$ depends on the input power through the dependence of carrier density $\bar{N}$ on $P_{\rm in}$. As will become evident in the appendix, specifying $r_{\rm FCD}$ for a power level different than 40 mW is a simple matter as $\bar{N}$ scales with $P_{\rm in}^2$.

TABLE I
VALUES OF PARAMETERS IN EQS. (11), (12) FOR SYSTEM UNDER STUDY

Parameter	Value
$r_{\rm TPA}$	0.0095
$r_{\rm FCD}$ ($\tau_c = 8$ ps)	0.0294 ($P_{\rm in} = 40$mW)
$r_{\rm FCA}$ ($\tau_c = 8$ ps)	0.0019
$r_{\rm FCD}^{\rm dyn}$	$0.0206 + 0.0972\bar{n}^{-0.2}$
$r_{\rm FCA}^{\rm dyn}$	0.0042

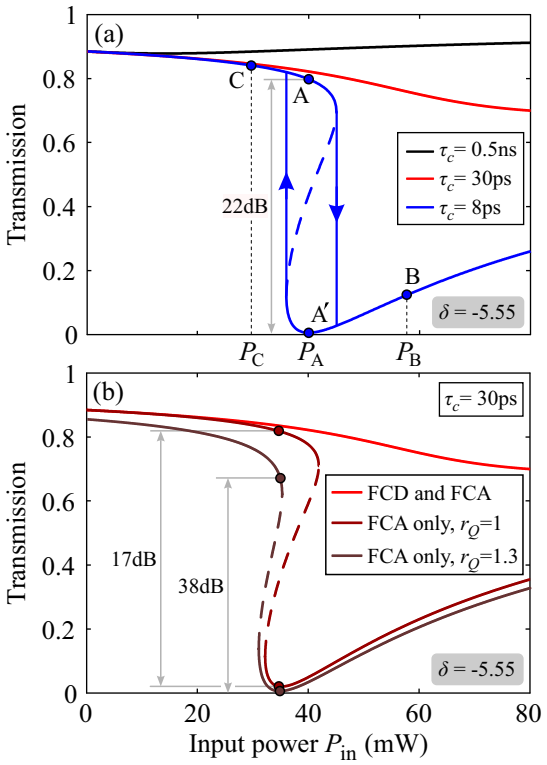

Fig. 7. Bistability curves for the optimum disk-resonator system ($R = 1.158$ μm, $g = 400$ nm). (a) Effect of carrier lifetime: FCEs have a detrimental effect on the nonlinear response preventing the manifestation of bistability for $\tau_c = 0.5$ ns. Carrier lifetime must drop to 8 ps for a good bistability loop to form. The onset of bistability is approximately 40 mW and a maximum ER of 22 dB is measured between points A and A′. Points B, C are used in Fig. 8 for toggling between them. (b) For a carrier lifetime of 30 ps it is FCD that hinders bistability manifestation. FCA is weak and the resulting ER degradation can be readily compensated by tuning the r_Q value.

Let us now investigate the effect of free carriers on the bistability curve by solving (11). For a typical carrier lifetime for submicron waveguides of 0.5 ns, no loop can be observed whatsoever (Fig. 7). Carrier lifetime must drop to 8 ps for a loop with good characteristics, i.e., high ER between bistable states and wide span, to appear. Such a carrier lifetime can perhaps be attained through carrier sweeping; recent studies

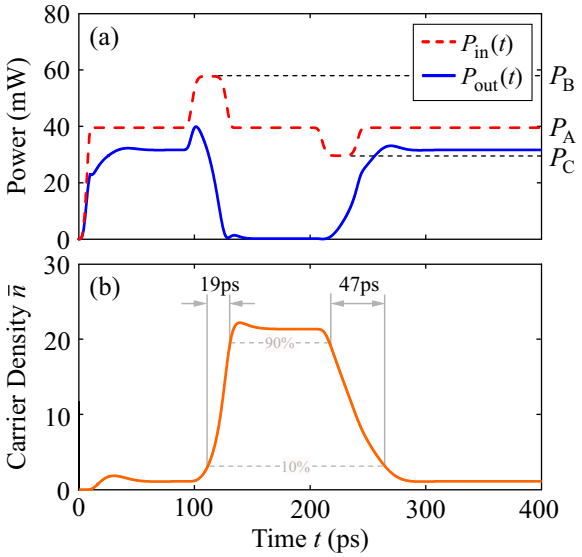

Fig. 8. Temporal response of the optimum disk-resonator system ($R = 1.158$ μm, $g = 400$ nm) with $\tau_c = 8$ ps and $\delta = -5.55$. (a) Basic memory operation is demonstrated with set/reset pulses toggling the system to the low-output state (through route ABA′ on the bistability curve) and then back to the high-output state (A′CA route). Points A, B, A′, and C are clearly marked in Fig. 7(a). (b) Evolution of the normalized carrier density. Rise time is limited by the cavity photon lifetime τ_ℓ and equals 19 ps, whereas fall time is determined by both carrier and cavity lifetimes and equals 47 ps.

have demonstrated lifetimes as low as 12 ps with moderate biasing voltages [22]. Notice that the onset of bistability is approximately 40 mW ($8P_0^{\rm Kerr}$), instead of 28 mW in Fig. 6, meaning that despite the significantly reduced carrier lifetime FCEs have not been completely suppressed. This is also confirmed by the maximum ER which equals 22 dB, instead of 31 dB in Fig. 6.

Both FCD and FCA are responsible for preventing bistability to manifest when $\tau_c = 0.5$ ns. FCD induces a frequency shift acting against the Kerr effect (opposite-sign shifts), whereas FCA, as with any loss mechanism, reduces the height and width of the bistability region until a loop is no longer observable. In our case, FCD is the most restricting of the two. This is demonstrated in Fig. 7(b) with a carrier lifetime of 30 ps. More specifically, when both FCD and FCA are considered bistability does not manifest. On the other hand, when only FCA is considered a clear bistability loop is formed. The maximum ER in the bistability region is 17 dB; it is not infinite due to FCA and, in a lesser extent, TPA loss (cf. Fig. 6). As already mentioned, this can be amended by tuning r_Q to satisfy the condition $Q_e^{-1} = Q_i^{-1} + Q_{\rm TPA}^{-1} + Q_{\rm FCA}^{-1}$, instead of $Q_e = Q_i$ ($r_Q = 1$). More specifically, by setting $r_Q = 1.3$ (it corresponds to $g = 383$ nm, Fig. 5) the ER becomes 38 dB. Through a finer adjustment of r_Q we can fully compensate the ER degradation due to FCA and TPA, reaching arbitrarily high (theoretically infinite) values. Although the procedure was demonstrated for the case without FCD, it obviously holds when FCD is present, i.e., tuning r_Q can also boost the ER of the $\tau_c = 8$ ps curve in Fig. 7(a).

High-quality bistable response, like the one depicted in Fig. 7(a) for $\tau_c = 8$ ps, can be exploited in practical applications. For example, in Fig. 8(a) we demonstrate ultrafast memory operation using third-order super-Gaussian set and reset pulses with a FWHM of 26 ps. The first pulse peaking at $P_{\rm B}$ [Fig. 7(a)] toggles the system to the low-output state (A′), whereas the second exploits point C below the bistable region to toggle the system back to the high-output state (A). The evolution of carrier density is also presented, Fig. 8(b). Rise (10%-90%) and fall (90%-10%) times are clearly noted and equal 19 and 47 ps, respectively. Carriers are generated *instantaneously* through TPA. Therefore, carrier rise time should closely follow the pulse rise time, which is 7 ps. However, the rate at which the cavity can fill with light is limited by the loaded cavity lifetime $\tau_\ell = \tau_i/2 = 8.8$ ps, which in our case is more restrictive. Therefore, we expect a rise time of $\ln(9)\tau_\ell = 19.4$ ps which agrees well with the 19 ps measured in Fig. 8(b). On the other hand, carriers do not recombine instantaneously (the carrier lifetime is finite); carrier fall time is determined by both carrier and cavity lifetimes and equals 47 ps. The disparity in carrier rise and fall times is reflected on the output power with the first transition happening faster than the second [Fig. 8(a)]. However, in both cases the system settles at the new state in less than 50 ps. As a result, memory operation with rates exceeding 10 Gbps is possible. Finally, we note that by employing a second signal near a different cavity resonance more elaborate functions can be demonstrated such as on-off switching and logic-gate functions [3]–[5].

IV. Self Pulsation

When carrier and cavity lifetimes are of the same order of magnitude, self-pulsation can manifest [23], [24]. In our case, the cavity photon lifetime of the uncoupled disk is $\tau_i = 17.6$ ps ($Q_i = \omega_0\tau_i/2$ with $Q_i = 10720$). Therefore, in the process of suppressing FCEs by lowering the carrier lifetime in Section III-C we come by a regime where τ_c is comparable with τ_i and carrier effects are strong enough to result in SP.

More specifically, depending on the carrier lifetime we can distinguish between regimes where only SP or SP *and* FCD-induced BI are possible. This is clearly demonstrated in Fig. 9 where four different values of the normalized carrier lifetime $\tau_c' = \tau_c/\tau_i$ are investigated. (Details on how the SP/BI regions are specified in Fig. 9 can be found in the appendix.) For $\tau_c' = 0.45$ ($\tau_c = 8$ ps), FCD has been significantly suppressed and only Kerr-induced BI is observed, Fig. 9(a). The rest point, $P_{\rm in} = P_A$, used for demonstrating memory operation in Fig. 8(a) is marked with a star. A clear SP region appears for $\tau_c' = 1.5$, Fig. 9(b). It spans negative detunings only and extends to input powers as low as 25 mW. Note that BI does not manifest since Kerr and FCD effects induce comparable frequency shifts that cancel each other out. In Fig. 9(c), $\tau_c' = 2.5$, the SP region broadens and extends to positive detunings as well. The FCD-induced frequency shift exceeds the Kerr counterpart resulting in FCD-induced bistability. Note the stars marking points inside and outside the SP region that will be used in Fig. 10 for demonstrating oscillating and stable operation, respectively. Finally, for $\tau_c' = 4.5$, Fig. 9(d), we again observe both SP and FCD-induced bistability regions. This time, the two regions overlap; in the intersection we get bistable behavior with the operating points lying on one

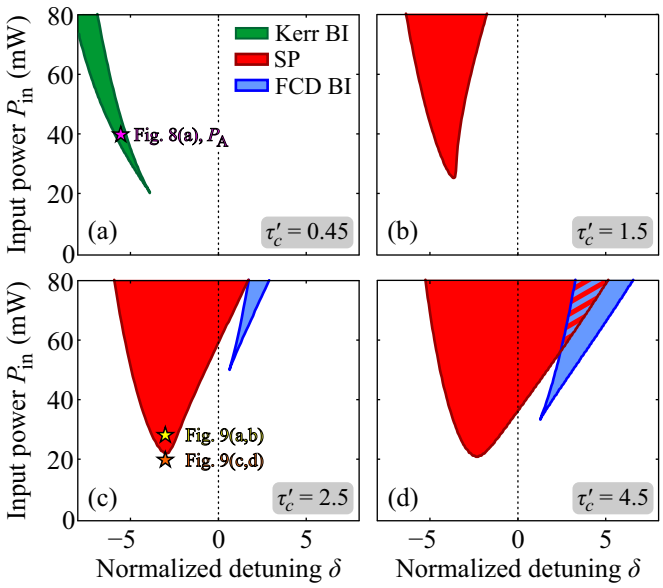

Fig. 9. BI and SP regions for different carrier lifetimes. (a) $\tau_c' = 0.45$ ($\tau_c = 8$ ps): FCD is weak due to the short carrier lifetime. Only Kerr-induced BI is observed. A star marks the point used for demonstrating memory operation in Fig. 8(a). (b) $\tau_c' = 1.5$: SP manifests for negative detunings only. (c) $\tau_c' = 2.5$: Non-overlapping SP and FCD-induced BI regions. SP extends to positive detunings as well. Stars mark points used in Fig. 10 for demonstrating oscillating and stable operation. (d) $\tau_c' = 4.5$: Overlapping SP and FCD-induced BI regions. As τ_c' increases, FCD becomes stronger and the corresponding BI manifests for lower input powers.

branch leading to stable output and those lying on the other to oscillating output [23]. Note also that as τ_c' increases, FCD becomes stronger and BI manifests for lower input powers.

By observing Fig. 9 one can readily verify that Kerr-induced BI appears for negative detunings, whereas FCD-induced BI for positive detunings. This is because of the opposite sign of the respective frequency shifts. On the other hand, SP can span both negative and positive detunings, as shown in Fig. 9(c,d).

In Fig. 10 we investigate the characteristics of SP oscillations in the temporal domain by solving (12). Two different input power levels are considered, inside and outside the SP region, respectively. They are clearly marked in Fig. 9(c) ($\tau_c' = 2.5$) and correspond to $\delta = -3$. For an input power of 27.2 mW, inside the SP region, we obtain an oscillating output, Fig. 10(a). The periodic response is highlighted by the limit cycle formed in the phase-space diagram of the normalized cavity amplitude $\tilde{u}$ [inset in Fig. 10(b)]. The non-circular shape indicates deviation from a sinusoidal response, something attributed to the Kerr effect. Regarding oscillation characteristics, we find a frequency of 7.5 GHz and a high modulation depth of 0.8, calculated through $(P_{\text{out}}^{\max} - P_{\text{out}}^{\min})/(P_{\text{out}}^{\max} + P_{\text{out}}^{\min})$. On the other hand, for an input power of 21.2 mW, outside the SP region [Fig. 9(c)], the spontaneous oscillation cannot be sustained and the output power eventually reaches a constant value. This is highlighted by the spiral shape in the phase-space diagram [inset in Fig. 10(d)].

As with bistable operation, self-pulsation can also be exploited in practical applications. For example, as indicated by Fig. 10(a) we can design an integrated clock operating with an input power below 30 mW and considerable modulation

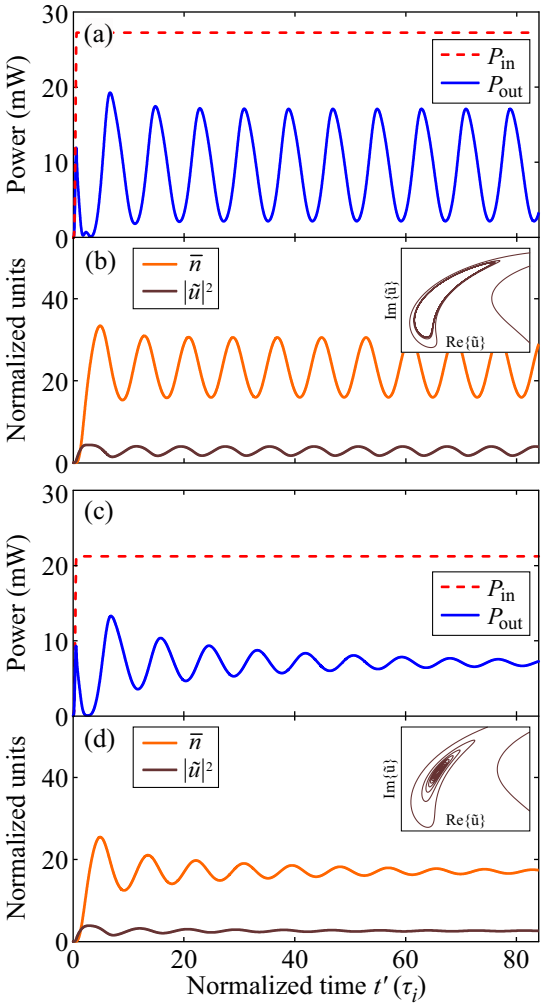

Fig. 10. Temporal response for two different P_{in} levels inside and outside the SP region. They are clearly marked in Fig. 9(c) ($\tau_c' = 2.5$) and correspond to $\delta = -3$. Top panels depict input and output power, whereas bottom panels depict normalized carrier density and stored energy. (a,b) Self-pulsation for $P_{\text{in}} = 27.2$ mW. The periodic response is highlighted by the limit cycle formed in the phase-space diagram [inset in (b)]. The non-circular shape indicates deviation from a sinusoidal waveform, something attributed to the Kerr effect. (c,d) $P_{\text{in}} = 21.2$ mW: The system eventually reaches a stable state as indicated by the spiral shape in the phase-space diagram [inset in (d)].

depth. The oscillating frequency can be tuned by varying the input power [24]. More specifically, varying P_{in} in the range 25-45 mW, the oscillating frequency is tuned from 7.15 to 9 GHz, while maintaining a fairly sinusoidal waveform with a modulation depth exceeding 0.8 in the entire range.

V. Conclusion

To summarize, we have proposed a hybrid plasmonic disk-waveguide configuration for Kerr bistability and self pulsation, operating with mW input powers. Such power requirements would have been deemed impossible with plasmonics a few years ago (early works in nonlinear plasmonics mentioned W or even kW power levels), due to the accompanying resistive losses. They have been made possible by a favorable combination of the nanoscale confinement offered by HPWs (metal/low-index dielectric/high-index dielectric layer configuration) with the reduced resistive losses of long-range modes

(symmetric waveguiding environment). We stress that other, more developed nanophotonic technologies do not provide lower input power requirements when it comes to Kerr-induced bistability (see for example [17]). Low-power bistable switching in silicon photonics for example relies on carrier [4] or thermal [3] nonlinearities instead of the Kerr effect, since such effects are associated with lower CW power thresholds for the particular structures examined. However, the response time in these cases is in the ns/μs range and cannot compete with the ps response of the current, Kerr-based approach. This also means that a comparison of CW power levels is not exactly fair since response times and bit rates differ significanlty; rather, it is safer to compare switching energies (per bit) for specific memory/switching operations. It is the ability of LRHPWs to accommodate the supported mode in nanometer-sized gaps hosting a highly-nonlinear $\chi^{(3)}$ material while maintaining propagation losses at a minimum that permits such high values of resonator nonlinearity ($\kappa_{\rm Kerr}$) and, thus, ultrafast, Kerr-induced bistability with mW input powers.

We have demonstrated high-quality bistable response leading to ultrafast (10 Gbps) memory operation with low input power requirements ($\sim$40 mW) and high ER (>20 dB) between states. For this to happen, carrier lifetime must drop to 8 ps in order to suppress FCA and, more importantly, FCD. Such lifetimes can perhaps be attained through carrier sweeping. Alternatively, different material systems that do not suffer from TPA can be examined (e.g., III-V semiconductors, chalcogenide glasses, etc.), provided that an adequately strong index contrast between low-index/high-index regions is attained. In addition, we have demonstrated self-pulsing behavior by properly tuning the carrier lifetime. For $\tau_c = 44$ ps, the oscillations feature considerable modulation depth (>0.8) and a frequency which can vary between 7.15 to 9 GHz by tuning the input power in the range 25-45 mW.

For the numerical analysis a theoretical framework based on perturbation theory and coupled-mode theory was employed, incorporating all relevant effects: Kerr, TPA, FCD, and FCA. For an even more comprehensive analysis one would have to include thermo-optic effects as well, stemming from Joule heating, TPA, and FCA. Such effects induce strong index changes [21], but (fortunately) not losses. In CW operation they can substantially impact the system response, leading themselves to bistable behavior. However, in the context of ultrafast dynamic operation, such as the memory operation demonstrated in Section III-C (Fig. 8), their effect is marginal. More specifically, since their response time is dictated by thermal diffusion, anticipated time constants are in the μs range. This means that they cannot follow the changes in stored energy induced from ps-long set and reset pulses. As a result, thermal frequency shifts are constant with time. Therefore, obtaining the memory operation of Fig. 8 in the presence of thermal effects is simply a matter of properly selecting the detuning in order to account for the constant thermo-optic frequency shifts. This was not possible with FCD, which had to be suppressed by tuning the carrier lifetime, since although carriers recombine with ns lifetimes, they are generated instantaneously.

APPENDIX
INTRODUCING FREE-CARRIER EFFECTS IN CMT FRAMEWORK

In this appendix, we show how FCEs are introduced in the CMT framework and specify all parameters appearing in equations (11) and (12) presented in Sec. III-C. As is well known, free carriers affect the *linear* susceptibility of Si (both real and imaginary parts) through

$$\Delta\chi^{(1)}_{\rm FCE} = 2n\Delta n_{\rm FCD} - j\frac{nc_0}{\omega}\Delta a_{\rm FCA}, \tag{13}$$

where [25]

$$\Delta n_{\rm FCD} = -\sigma_n^e N - (\sigma_n^h N)^{0.8}, \tag{14a}$$
$$\Delta a_{\rm FCA} = +\sigma_a N, \tag{14b}$$

with $\sigma_n^e = 8.8\times10^{-28}$ m^3, $\sigma_n^h = 4.6\times10^{-28}$ m^3, and $\sigma_a = 14.5\times10^{-22}$ m^2. N (measured in m^{-3}) is the coordinate-dependant electron/hole density (TPA generates electrons and holes in equal proportions, $N_e = N_h \equiv N$), governed by

$$\frac{{\rm d}N}{{\rm d}t} = -\frac{N}{\tau_c} + \frac{1}{2\hbar\omega_0}\frac{{\rm d}P_{\rm TPA}}{{\rm d}V}, \tag{15}$$

with ${\rm d}P_{\rm TPA}/{\rm d}V$ given by (5).

Using first-order perturbation theory [18], [21], we can calculate the correction $\Delta\omega_{\rm FCE}$ due to FCs on the unperturbed resonant frequency ω_0:

$$\frac{\Delta\omega_{\rm FCE}}{\omega_0} = -\frac{1}{2}\frac{\iiint_V \Delta\chi^{(1)}_{\rm FCE}|\mathbf{E}_0|^2{\rm d}V}{\iiint_V n^2|\mathbf{E}_0|^2{\rm d}V}. \tag{16}$$

$\Delta\omega_{\rm FCE}$ is a complex quantity; its real part describes the resonant frequency shift due to FCD ($\Delta\omega_{\rm FCD} = {\rm Re}\{\Delta\omega_{\rm FCE}\}$) and its imaginary part the losses due to FCA ($\tau^{-1}_{\rm FCA} = {\rm Im}\{\Delta\omega_{\rm FCE}\}$). $\Delta\omega_{\rm FCD}$ and $\tau^{-1}_{\rm FCA}$ can be directly introduced in the CMT formalism for describing the effect of FCD and FCA, respectively, just as $\Delta\omega$ and $\tau^{-1}_{\rm TPA}$ describe the effect of Kerr and TPA in (1a). In what follows, we specify these terms for both CW and dynamic conditions and outline the normalization procedure followed for arriving at (11), (12).

A. CW Conditions

First, let us assume CW conditions. This means that ${\rm d}N/{\rm d}t = 0$ in (15) and $N(\mathbf{r}) = (\tau_c/2\hbar\omega_0){\rm d}P_{\rm TPA}/{\rm d}V$. Subsequently, we approximate (14a) by $\Delta n_{\rm FCD} = -\sigma_n N$, where $\sigma_n = \sigma_n^e + (\sigma_n^h)^{0.8}\bar{N}^{-0.2}$ is rendered spatially constant by making use of $\bar{N}$: a weighted spatially-averaged carrier density, instead of the coordinate-dependent N, defined through

$$\bar{N} = \frac{\iiint_V N(\mathbf{r})|\mathbf{E}_0(\mathbf{r})|^2{\rm d}V}{\iiint_V |\mathbf{E}_0(\mathbf{r})|^2{\rm d}V}. \tag{17}$$

Considering the above, by plugging (13) into (16) we find $\Delta\omega_{\rm FCD}=\gamma_{\rm FCD}W^2$ and $\tau_{\rm FCA}^{-1}=\gamma_{\rm FCA}W^2$, where

$$\gamma_{\rm FCD}=\frac{1}{16}\left(\frac{\omega_0}{c_0}\right)^6\frac{\sigma_n(\bar{N})\tau_c c_0^2}{\hbar}\kappa_{\rm FCE}\beta_{\rm TPA}^{\max}, \tag{18a}$$

$$\gamma_{\rm FCA}=\frac{1}{32}\left(\frac{\omega_0}{c_0}\right)^6\frac{\sigma_a\tau_c c_0^3}{\hbar\omega_0}\kappa_{\rm FCE}\beta_{\rm TPA}^{\max}, \tag{18b}$$

are nonlinear parameters measured in $\mathrm{W}^{-2}\mathrm{s}^{-3}$. In (18) we have defined the nonlinear feedback parameter $\kappa_{\rm FCE}$ as

$$\kappa_{\rm FCE}\triangleq\left(\frac{c_0}{\omega_0}\right)^6\times\frac{\frac{1}{3}\iiint_V\beta_{\rm TPA}n^3\left[|\mathbf{E}_0\cdot\mathbf{E}_0|^2+2|\mathbf{E}_0|^4\right]|\mathbf{E}_0|^2\mathrm{d}V}{\left[\frac{1}{2}\iiint_V n^2|\mathbf{E}_0|^2\mathrm{d}V\right]^3\beta_{\rm TPA}^{\max}}. \tag{19}$$

As mentioned in [24], [26], normalizing the CMT equations is essential for obtaining robust numerical solutions. Since we focus on Kerr-induced bistability, we normalize the involved quantities with respect to $P_0^{\rm Kerr}$. To this end, we normalize wave and cavity amplitudes by defining $\tilde{\psi}_i=\tilde{s}_i/\sqrt{P_0^{\rm Kerr}}$ and $\tilde{u}=\sqrt{\tau_i\gamma_{\rm Kerr}}\tilde{a}$, respectively. For the FCE terms we get

$$r_{\rm FCD}=\frac{\gamma_{\rm FCD}}{\tau_i\gamma_{\rm Kerr}^2}=\frac{\sigma_n(\bar{N})\tau_c}{\tau_i\omega_0^2\hbar}\,\frac{\kappa_{\rm FCE}\beta_{\rm TPA}^{\max}}{\kappa_{\rm Kerr}^2\left(n_2^{\max}\right)^2}, \tag{20a}$$

$$r_{\rm FCA}=\frac{\gamma_{\rm FCA}}{\tau_i\gamma_{\rm Kerr}^2}=\frac{\sigma_a\tau_c c_0}{2\tau_i\omega_0^3\hbar}\,\frac{\kappa_{\rm FCE}\beta_{\rm TPA}^{\max}}{\kappa_{\rm Kerr}^2\left(n_2^{\max}\right)^2}. \tag{20b}$$

Note that $r_{\rm FCD}$ depends on $\bar{N}$ through σ_n and, therefore, on the input power. In Table I we present a value corresponding to $P_{\rm in}=40$ mW. More specifically, feeding the bus waveguide with this power level, while assuming critical coupling conditions and an operating wavelength coinciding with the cavity resonance, we find $\bar{N}=1.6\times10^{24}\ \mathrm{m}^{-3}$ in the resonator. Using this value we get $\sigma_n=2.7\times10^{-27}\ \mathrm{m}^3$ and $r_{\rm FCD}=0.0294$. Specifying $r_{\rm FCD}$ for any other power level is a simple matter as $\bar{N}$ scales with $P_{\rm in}^2$.

B. Pulsed Conditions

Let us now switch to the dynamic case. Introducing $\bar{N}$ in Eq. (15) we get

$$\frac{\mathrm{d}\bar{N}}{\mathrm{d}t}=-\frac{\bar{N}}{\tau_c}+\gamma_N|\tilde{a}|^4, \tag{21}$$

with

$$\gamma_N=\frac{1}{8}\left(\frac{\omega_0}{c_0}\right)^6\frac{c_0^2}{\hbar\omega_0}\kappa_N\beta_{\rm TPA}^{\max}, \tag{22}$$

measured in $\mathrm{W}^{-2}\mathrm{s}^{-3}\mathrm{m}^{-3}$, and

$$\kappa_N\triangleq\left(\frac{c_0}{\omega_0}\right)^6\times\frac{\frac{1}{3}\iiint_V\beta_{\rm TPA}n^2\left[|\mathbf{E}_0\cdot\mathbf{E}_0|^2+2|\mathbf{E}_0|^4\right]|\mathbf{E}_0|^2\mathrm{d}V}{\iiint_V|\mathbf{E}_0|^2\mathrm{d}V\left[\frac{1}{2}\iiint_V n^2|\mathbf{E}_0|^2\mathrm{d}V\right]^2\beta_{\rm TPA}^{\max}}. \tag{23}$$

Using again (13) in (16) we find $\Delta\omega_{\rm FCD}^{\rm dyn}=\gamma_{\rm FCD}^{\rm dyn}\sigma_n(\bar{N})\bar{N}$ and $(\tau_{\rm FCA}^{\rm dyn})^{-1}=\gamma_{\rm FCA}^{\rm dyn}\bar{N}$, representing dynamic frequency shift and loss due to FCEs. The fact that the dynamic versions of $\Delta\omega_{\rm FCD}$, $\tau_{\rm FCA}$ are functions of $\bar{N}$ instead of W^2 should not come as a surprise, as the driving term in (21) directly depends on $|a|^4$, i.e., W^2. The nonlinear parameters $\gamma_{\rm FCD}^{\rm dyn}$, $\gamma_{\rm FCA}^{\rm dyn}$ are the dynamic counterparts of $\gamma_{\rm FCD}$, $\gamma_{\rm FCA}$ and are given by

$$\gamma_{\rm FCD}^{\rm dyn}=\frac{1}{2}\omega_0\frac{\kappa_{\rm FCE}}{\kappa_N}, \tag{24a}$$

$$\gamma_{\rm FCA}^{\rm dyn}=\frac{1}{4}c_0\frac{\kappa_{\rm FCE}}{\kappa_N}\sigma_a. \tag{24b}$$

To reach (12), we normalize $\bar{N}$ through $\bar{n}=(\tau_i\gamma_{\rm Kerr}^2/\gamma_N)\bar{N}$ ($\tilde{u}$ and $\tilde{\psi}_i$ as in the CW case). Using, in addition, τ_i as the time unit (i.e., $t'=t/\tau_i$ and $\tau_c'=\tau_c/\tau_i$) we find

$$r_{\rm FCD}^{\rm dyn}(\bar{n})=\frac{r_{\rm FCD}}{\tau_c'}, \tag{25a}$$

$$r_{\rm FCA}^{\rm dyn}=\frac{r_{\rm FCA}}{\tau_c'}. \tag{25b}$$

One can verify that $r_{\rm FCD/FCA}^{\rm dyn}$ do not depend on the carrier lifetime, since $r_{\rm FCD/FCA}\propto\tau_c$ [Eq. (20)]. The values of $r_{\rm FCD/FCA}^{\rm dyn}$ for the system under study are compiled in Table I and are used for producing the results depicted in Figs. 8, 10.

Finally, let us briefly show how (12) is used for obtaining the SP/BI regions in Fig. 9. A linear stability analysis is conducted on the steady-state solutions of these equations, as discussed in [23], [24], [26]. Letting $\tilde{u}'=\tilde{u}+\delta\tilde{u}$ and $\bar{n}'=\bar{n}+\delta\bar{n}$, the perturbation array $\boldsymbol{\varepsilon}\equiv[\delta\tilde{u}\ \ \delta\tilde{u}^*\ \ \delta\bar{n}]^{\mathrm{T}}$ is found to satisfy $\mathrm{d}\boldsymbol{\varepsilon}/\mathrm{d}t'=J\boldsymbol{\varepsilon}$ with

$$J=\begin{bmatrix}J_1 & J_2 & J_3\\ J_2^* & J_1^* & J_3^*\\ J_4 & J_4^* & J_5\end{bmatrix}, \tag{26}$$

where $J_1=j(-\delta-2|\tilde{u}|^2+r_{\rm FCD}^{\rm dyn}(\bar{n})\bar{n})-(1+r_Q+2r_{\rm TPA}|\tilde{u}|^2+r_{\rm FCA}^{\rm dyn}\bar{n})$, $J_2=-j\tilde{u}^2-r_{\rm TPA}\tilde{u}^2$, $J_3=jr_{\rm FCD}^{\rm dyn}(\bar{n})\tilde{u}-r_{\rm FCA}^{\rm dyn}\tilde{u}$, $J_4=2\tilde{u}^*|\tilde{u}|^2$ and $J_5=-1/\tau_c'$. The eigenvalues of (26) determine the limits of BI and SP regions as discussed in [23], [24], [26]. In addition, they characterize the SP oscillations: the oscillation frequency is proportional to the imaginary part.

REFERENCES

[1] M. Kauranen and A. V. Zayats, "Nonlinear plasmonics," *Nat. Photon.*, vol. 6, no. 11, pp. 737–748, Nov 2012.
[2] T. Tanabe, M. Notomi, S. Mitsugi, A. Shinya, and E. Kuramochi, "Fast bistable all-optical switch and memory on a silicon photonic crystal on-chip," *Opt. Lett.*, vol. 30, no. 19, pp. 2575–2577, Oct 2005.
[3] M. Notomi, A. Shinya, S. Mitsugi, G. Kira, E. Kuramochi, and T. Tanabe, "Optical bistable switching action of Si high-Q photonic-crystal nanocavities," *Opt. Express*, vol. 13, no. 7, pp. 2678–2687, Apr. 2005.
[4] Q. Xu and M. Lipson, "All-optical logic based on silicon micro-ring resonators," *Opt. Express*, vol. 15, no. 3, pp. 924–929, Feb 2007.
[5] P. Sethi and S. Roy, "All-optical ultrafast switching in 2×2 silicon microring resonators and its application to reconfigurable demux/mux and reversible logic gates," *J. Lightw. Technol.*, vol. 32, no. 12, pp. 2173–2180, Jun 2014.
[6] O. Tsilipakos and E. E. Kriezis, "Optical bistability with hybrid silicon-plasmonic disk resonators," *J. Opt. Soc. Am. B*, vol. 31, no. 7, pp. 1698–1705, Jul 2014.
[7] T. Christopoulos, G. Sinatkas, O. Tsilipakos, and E. E. Kriezis, "Bistable action with hybrid plasmonic Bragg-grating resonators," *Opt. Quantum Electron.*, submitted.

[8] Y. Bian, Z. Zheng, X. Zhao, J. Zhu, and T. Zhou, "Symmetric hybrid surface plasmon polariton waveguides for 3D photonic integration," *Opt. Express*, vol. 17, no. 23, pp. 21 320–21 325, Nov 2009.
[9] Y. Binfeng, H. Guohua, J. Yang, and C. Yiping, "Characteristics analysis of a hybrid surface plasmonic waveguide with nanometric confinement and high optical intensity," *J. Opt. Soc. Am. B*, vol. 26, no. 10, pp. 1924–1929, Oct 2009.
[10] P. Berini, "Plasmon-polariton waves guided by thin lossy metal films of finite width: Bound modes of symmetric structures," *Phys. Rev. B*, vol. 61, no. 15, pp. 10 484–10 503, Apr. 2000.
[11] W. Wei, X. Zhang, and X. Ren, "Guiding properties of asymmetric hybrid plasmonic waveguides on dielectric substrates," *Nanoscale Res. Lett.*, vol. 9, no. 13, pp. 1–6, Jul 2014.
[12] W. Ma and A. S. Helmy, "Asymmetric long-range hybrid-plasmonic modes in asymmetric nanometer-scale structures," *J. Opt. Soc. Am. B*, vol. 31, no. 7, pp. 1723–1729, Jul 2014.
[13] B. Esembeson, M. L. Scimeca, T. Michinobu, F. Diederich, and I. Biaggio, "A high-optical quality supramolecular assembly for third-order integrated nonlinear optics," *Adv. Mater.*, vol. 20, no. 23, pp. 4584–4587, 2008.
[14] P. B. Johnson and R. W. Christy, "Optical constants of the noble metals," *Phys. Rev. B*, vol. 6, no. 12, pp. 4370–4379, Dec 1972.
[15] A. Boltasseva, T. Nikolajsen, K. Leosson, K. Kjaer, M. Larsen, and S. Bozhevolnyi, "Integrated optical components utilizing long-range surface plasmon polaritons," *J. Lightw. Technol.*, vol. 23, no. 1, pp. 413–422, 2005.
[16] O. Tsilipakos, D. C. Zografopoulos, and E. E. Kriezis, "Quasi-soliton pulse-train propagation in dispersion-managed silicon rib waveguides," *IEEE Photon. Technol. Lett.*, vol. 25, no. 8, pp. 724–727, 2013.
[17] M. Soljačić, M. Ibanescu, S. G. Johnson, Y. Fink, and J. D. Joannopoulos, "Optimal bistable switching in nonlinear photonic crystals," *Phys. Rev. E*, vol. 66, no. 5, p. 055601, Nov. 2002.
[18] J. Bravo-Abad, S. Fan, S. Johnson, J. D. Joannopoulos, and M. Soljačić, "Modeling nonlinear optical phenomena in nanophotonics," *J. Lightw. Technol.*, vol. 25, no. 9, pp. 2539–2546, 2007.
[19] O. Tsilipakos, A. Pitilakis, A. C. Tasolamprou, T. V. Yioultsis, and E. E. Kriezis, "Computational techniques for the analysis and design of dielectric-loaded plasmonic circuitry," *Opt. Quantum Electron.*, vol. 42, no. 8, pp. 541–555, Jul. 2011.
[20] B. Maes, P. Bienstman, and R. Baets, "Switching in coupled nonlinear photonic-crystal resonators," *J. Opt. Soc. Am. B*, vol. 22, no. 8, pp. 1778–1784, Aug. 2005.
[21] J. Wang, L. Fan, L. T. Varghese, H. Shen, Y. Xuan, B. Niu, and M. Qi, "A theoretical model for an optical diode built with nonlinear silicon microrings," *J. Lightw. Technol.*, vol. 31, no. 2, pp. 313–321, Jan. 2013.
[22] A. C. Turner-Foster, M. A. Foster, J. S. Levy, C. B. Poitras, R. Salem, A. L. Gaeta, and M. Lipson, "Ultrashort free-carrier lifetime in low-loss silicon nanowaveguides," *Opt. Express*, vol. 18, no. 4, pp. 3582–3591, Feb. 2010.
[23] S. Malaguti, G. Bellanca, A. de Rossi, S. Combrié, and S. Trillo, "Self-pulsing driven by two-photon absorption in semiconductor nanocavities," *Phys. Rev. A*, vol. 83, p. 051802, May 2011.
[24] S. Chen, L. Zhang, Y. Fei, and T. Cao, "Bistability and self-pulsation phenomena in silicon microring resonators based on nonlinear optical effects," *Opt. Express*, vol. 20, no. 7, pp. 7454–7468, Mar 2012.
[25] R. A. Soref and B. Bennett, "Electrooptical effects in silicon," *IEEE J. Quant. Electron.*, vol. 23, no. 1, pp. 123–129, Jan 1987.
[26] L. Zhang, Y. Fei, T. Cao, Y. Cao, Q. Xu, and S. Chen, "Multibistability and self-pulsation in nonlinear high-Q silicon microring resonators considering thermo-optical effect," *Phys. Rev. A*, vol. 87, p. 053805, May 2013.